

**Bias Correction and Random Error Characterization for the Assimilation of  
HRDI Line-of-Sight Wind Measurements**

**Andrew Tangborn**

Data Assimilation Office NASA-GSFC, Code 910.3, Greenbelt, MD

and

JCET, University of Maryland-Baltimore County, Baltimore, MD

**Richard Menard**

Air Quality Research Branch, AES, Dorval, Canada

**David Ortland**

Northwest Research Associates, Bellevue, WA

Submitted to *Journal of Geophysical Research*

## 1 Abstract

A new approach to the analysis of systematic and random observation errors is presented in which the error statistics are obtained using forecast data rather than observations from a different instrument type. The analysis is carried out at an intermediate retrieval level, instead of the more typical state variable space. This method is carried out on measurements made by the High Resolution Doppler Imager (HRDI) on board the Upper Atmosphere Research Satellite (UARS). HRDI, a limb sounder, is the only satellite instrument measuring winds in the stratosphere, and the only instrument of any kind making global wind measurements in the upper atmosphere. HRDI measures doppler shifts in the two different  $O_2$  absorption bands ( $\alpha$  and B) and the retrieved products are tangent point Line-of-Sight wind component (level 2 retrieval) and UV winds (level 3 retrieval). This analysis is carried out on a level 1.9 retrieval, in which the contributions from different points along the line-of-sight have not been removed. Biases are calculated from O-F (observed minus forecast) LOS wind components and are separated into a measurement parameter space consisting of 16 different values. The bias dependence on these parameters (plus an altitude dependence) is used to create a bias correction scheme carried out on the level 1.9 retrieval. The random error component is analyzed by separating the  $\gamma$  and B band observations and locating observation pairs where both bands are very nearly looking at the same location at the same time. It is shown that the two observation streams are uncorrelated and that this allows the forecast error variance to be estimated. The bias correction is found to cut the effective observation error variance in half.

## 2 Introduction

This paper is about characterizing the instrument error, improving the bias correction scheme, and obtaining the statistical information necessary for the assimilation of line-of-sight (LOS) velocities of the High-Resolution Doppler Imager (HRDI). HRDI is on board the Upper Atmosphere Research Satellite (UARS), and is the first and currently the only satellite instrument providing direct global-scale measurements of the stratospheric wind field. Figure 3 shows a single day (September 1, 1994) of HRDI wind measurement coverage.

Accurate knowledge of stratospheric winds is especially important for chemical transport which has implications on global atmospheric chemistry and climate change (Rind and Lacis, 1993). Yet, stratospheric wind information has been traditionally indirect, obtained through model-driven assimilation of satellite temperature measurements. The exception are the few radiosondes that penetrate the tropopause, that is mainly over the tropics, and which provide wind measurements up to 35 km.

The wind information that can be obtained from data assimilation of temperature measurements depend to a large extent on the error covariance model. In most implementations of data assimilation schemes the error covariance models were developed for tropospheric assimilation. They have isotropic error correlations, assume geostrophy, and become univariate in the tropics (i.e. temperature and wind measurements are uncoupled). Error statistics in the stratosphere which are generally obtained by the lagged-forecast method (Parris and Derber, 1992) turn out not fit well the covariance model formulation and thus, shed some doubts on the effective use of temperature measurements in current implementation of stratospheric data assimilation schemes.

One of the most important use of the HRDI observations is then in the assimilation of the wind data to create an accurate portrait of stratospheric winds. These winds are particularly important for the creating high quality forecasts of chemical species in the stratosphere (Stajner, *et al.* 2000), (Menard *et al.* 2000(a,b)). It also helps to improve our knowledge of error statistics in the stratosphere. However, due to the complexity of the retrieval and the required accuracy of measurement, the HRDI retrieved (u,v) wind data have fairly large errors, both systematic and random, that exceeds the atmospheric signal. This significantly diminishes the impact of the HRDI winds on the Stratospheric analyses (Boorman, *et al.*

2000). To reduce both systematic and random errors, a bias correction scheme and a sequential estimation method along satellite tracks have been developed (Ortland *et al.* 1996). The sequential estimation method do, in particular, introduce a significant horizontal and vertical smoothing in the data product (Ortland *et al.* 1995).

In this study, we are for the assimilation the LOS velocities rather than the (u,v) wind retrieval. The primary quantity that is used in the bias correction and sequential estimation schemes are the LOS velocities, which are obtained by displacing and fitting a particular spectroscopic line shape. The assimilation of LOS velocities will avoid completely the use of the sequential estimation scheme, and should provide a better understanding of the observation error statistics. In preparation for the assimilation of the HRDI LOS velocities we have improved the bias correction scheme, and estimated the error variance of the different channels and viewing angles, as well as their correlation, and correlation with the forecast model output. In particular, we improved upon the bias correction scheme by adding a cold/warm side dependence, which in effect as also reduced the random error variance, and found that there is no correlation between the different channels and between the forecast error and observation error.

The organization of the paper goes as follows. In section 3 we describe how the LOS velocities are obtained and discuss the main sources of errors. In section 4 we how that observed-minus-forecast residuals can be used effectively to estimate the observation error bias, and improve upon the existing scheme. In section 5 using the method of maximum likelihood we obtain statistical information on the random error component. Finally a conclusion is given in section 6.

### 3 Description of the HRDI wind measurements

The HRDI measurements consist of counts on a 32-channel detector that represent the brightness in the spectrum of light entering the telescope at a discrete set of wavelengths. Measurements are taken while the HRDI telescope is pointed along a line of sight whose *tangent point* (the point closest to the center of the earth) is located at various altitudes within the stratosphere. The measured spectrum provides information on the wind in the atmosphere through the Doppler shift that this wind produces in the features of this spec-

trum. In order to deduce the wind from the measurements, a model of the instrument and the physical mechanisms that produce the spectral features must first be constructed. Errors in the wind determination arise from both random fluctuations in the detector counts and systematic errors that result from inaccurate knowledge of parameters in the model. Full details of the HRDI instrument and its operation may be found in Hays et al., (1993), Skinner et al. (1994) and Grassl et al., (1995), while details of the model and of the wind retrieval method may be found in Hays and Abreu (1989) and Ortland et al. (1995; 1996). This section summarizes those aspects of HRDI measurements that are important for understanding the nature of the systematic errors. The point of view used here for describing the retrieval of atmospheric properties from HRDI measurements is adopted from Rodgers (1990).

### 3.1 HRDI forward model

The relationship of the HRDI measurements to the atmospheric wind vectors is described in terms of the *forward model*  $\mathbf{y} = \mathbf{F}(\mathbf{x}, \mathbf{b}) + \epsilon$ , where  $\mathbf{y}$  is a *measurement vector* that represents the detector counts,  $\mathbf{x}$  is a *state vector* that represents the wind speed along the line of sight as a function of altitude, and  $\mathbf{b}$  is a vector that represents all the *model parameters* that are assumed to be known. These model parameters include such things as the instrument viewing geometry, the internal state of the instrument, and various properties of the atmosphere. All of the model parameters that significantly affect the determination of the winds will be described below. The vector  $\epsilon$  represents random fluctuations in the measurements, which for HRDI follows the Poisson statistics of photon counting, and is well known. The statistics of random errors in HRDI measurements will be examined in Section 5 below.

The signal detected by HRDI arises from sunlight scattered into the telescope field of view. The scattering is accomplished by the atmospheric gas molecules, aerosol particles, the earth surface and cloud tops. Along the route on its way from the sun to the telescope, some of the light is absorbed within a narrow range of wavelengths by  $\text{O}_2$  molecules, thereby producing the line shape measured by the HRDI instrument. The motion of both the absorbing  $\text{O}_2$  molecules and the particles that scatter light into the telescope field of view are responsible for the Doppler shift in the line shape that is used to determine the winds.

A single-scattering model, modified to take into account scattering from the earth surface,

is used to simulate the HRDI measurements. The single scattering approximation is accurate for the region of the atmosphere through which the HRDI line of sight passes. In the HRDI model, radiation that propagates up from the troposphere is treated as if it were reflected from a Lambertian surface with some effective albedo and height. The scattering and absorption properties of the atmosphere are characterized by scattering cross sections for the atmospheric molecules and aerosols, the scattering phase functions, which give the probability that light will be scattered at a particular angle, and absorption cross sections for the O<sub>2</sub> molecules. The aerosol and surface scattering properties are a function of latitude, longitude and altitude. The magnitudes of the absorption cross-sections are proportional to density, and the variation of the absorption cross section with wavelength depends on the atmospheric pressure. The pressure governs the width of the absorption line shape (pressure broadening), as well as the wavelength at which the line shape is centered (pressure shift). The viewing geometry is completely specified by the solar zenith angle, the scattering angle, and the LOS tangent height.

In addition to the single scattering model, which describes the physics of how light enters the HRDI telescope, a model of the instrument that describes the production of the signal on the detector is also required. In this model, the counts  $C_j$  produced on channel  $j$  of the instrument is represented in terms of the integral

$$C_j = \int I_j(\lambda - \lambda_0) B(\lambda) d\lambda \quad (1)$$

where  $I_j$  is the instrument response function and  $B$  is the brightness of light entering the telescope at wavelength  $\lambda$ . The *reference position*  $\lambda_0$  is a parameter that determines the location of the peak of the instrument response function, and thereby determines exactly where the spectral line shape will fall on the detector. The reference position does not depend on the channel number, but does depend on how the instrument is tuned, as described below. The exact value of the reference position is not known, and is the primary source of error in the HRDI forward model that this study seeks to eliminate. The reference position may also be considered to be a function of instrument temperature, which is precisely controlled and slowly varies as the UARS orbit precesses, as well as the relative motion of the satellite with respect to the earth. The dependence of the reference position on these parameters is

well known, and described in Grassl et al. (1995).

### 3.2 LOS velocity

The retrieval of the wind velocity components from HRDI measurements involves the construction of an *inverse model*  $x = I(y, b, c)$  expressed in terms of the same parameters as the forward model and an additional set of *inverse model parameters*  $c$ . The HRDI inverse model is derived from a least-squares fit of the forward model to the measurements. Because the inverse problem is underdetermined, a system of constraints is used to enforce smoothness conditions on the recovered profile and to constrain the small-scale structure of the recovered wind profile that cannot be determined from the measurements. The inverse model parameter vector  $c$  represents these constraints. Suppose that the wind profiles recovered in this way are used for data assimilation into a dynamical model. The wind field of the dynamical model will then not only be constrained to conform to the HRDI measurements, but will also be implicitly subject to the constraints that are part of the inverse model. Since this is undesirable, the best way to proceed is to use only the HRDI measurements together with the forward model as a means for constraining the assimilation model winds.

It is impractical, however, to use the HRDI measurements on the 32 channels as the data employed in the assimilation. This is because there are not 32 independent pieces of wind information contained in the measurements obtained from a single line of sight. To see this, consider the set of measurement vectors  $\mathbf{y}$  that is obtained under the forward model mapping  $\mathbf{y} = \mathbf{F}(\mathbf{x})$  by varying the state vector  $\mathbf{x}$  over all possible (and reasonable) wind profiles. This subset of the measurement vector lies close to a 1-dimensional subspace. In other words, variation of the wind profile mainly has the effect of shifting the measured spectrum on the detector without any significant change in its shape. Therefore, it is useful to distill the 32 measured values down to a single parameter that measures this shift.

The parameter that accomplished this is called *line-of-sight wind velocity*, or LOS velocity for short, and denoted  $V_{LOS}$ . The forward model is used to compute the reference line shape  $C_0(\lambda_i)$  that describes the brightness that would appear on channel  $i$  when the wind profile is uniformly zero, where  $\lambda_i$  is the wavelength at the center of the contribution function for channel  $i$ . The LOS velocity is determined by first finding the parameter  $\Delta\lambda$  that achieves

a best fit of the expression  $C_0(\lambda_i + \Delta\lambda)$  to the measurements  $C_i$ , and subsequently defined as  $V_{LOS} = c\Delta\lambda/\lambda_0$ , where  $c$  is the velocity of light and  $\lambda_0$  is the wavelength at the center of the spectral line. The LOS velocity determination is equivalent to fitting the forward model with a constant wind profile with wind speed  $v_{LOS}$ , and is also equivalent to specifying the location of the line center on the detector.

The LOS velocity  $V_{LOS}(z_{tan})$  can be related wind profile  $u(z_i)$  in the direction of the LOS via the formula:

$$V_{LOS}(z_{tan}) = \sum K(z_{tan}, z_i)u(z_i), \quad (2)$$

where  $z_{tan}$  is the tangent height of the line of sight, and the sum is over the set of altitude grid points  $z_i$  that are used to represent the velocity profile. The function  $K$  is called the LOS velocity kernel, and is obtained by linearization of the forward model about the zero wind profile. Figure 4 provides an example of the LOS kernel functions for a set of measurements in a full limb scan. The velocity kernel may be viewed as a set of weights that determine how much the wind at each altitude contributes to the value of  $V_{LOS}$ .

In the next section, HRDI LOS velocities will be compared to LOS velocities that are computed by substituting the GEOS velocity components along the line of sight for  $u$  in (2). Systematic differences between the HRDI and GEOS LOS velocities will be examined, and these differences will arise from either a systematic error in the HRDI or GEOS LOS velocity. The main goal of this paper will be to determine both the HRDI systematic error and the GEOS wind biases by means of these comparisons. A systematic error in the HRDI LOS velocity arises from inaccurate knowledge of the forward model parameters, and is a goal of this section to completely characterize how these systematic errors can arise. A systematic error in the GEOS LOS velocity will stem from either systematic bias in the GEOS winds or a systematic error in the LOS velocity kernel used to calculate the GEOS LOS velocity.

Errors in the GEOS LOS velocities that arise from the LOS velocity kernel will mainly be due to inaccurate knowledge of the properties of the aerosols and surface albedo. These atmospheric properties control the relative proportions of signal produced along the line of sight that reach the HRDI instrument. It is unlikely that the uncertainty in the aerosols and surface albedo is large enough to significantly affect the LOS velocity kernels. Moreover,



any inaccurate assignment of the LOS kernel weighting that does occur will only have a significant effect on the GESO LOS velocity if the GEOS wind profile has a large vertical shear. It is therefore unlikely that a significant error will appear in the global averages that are employed in this paper, and potential source of error in the GESO LOS velocities will subsequently be ignored.

### 3.3 HRDI mode of operation

The systematic errors in the HRDI LOS velocity that will be discussed below partially depend on the HRDI instrument configuration. This configuration is therefore described in detail in this subsection.

The HRDI telescope position is conveniently described via reference to a plane parallel to the surface of the earth and passing through the telescope gimbals at the origin. The x-axis in this plane may be defined as a line parallel to the UARS direction of motion, and fixed with respect to the body of the satellite. The telescope azimuth angle is measured in this plane relative to the x-axis so defined.

On any given day, the HRDI telescope performs a series of limb scans with the telescope pointed alternately at two different azimuth angles. The pair of angles either consists of 45/135 or 225/315 degrees. This provides a set of forward and backward looking lines of relative to the satellite velocity vector. These particular pairs of angles are chosen so as to provide orthogonal view directions and thereby enable the two components of the horizontal wind vector to be measured. They also imply that the tangent points of the lines of sight in the backward set coincide with the tangent points from the forward looking set taken 9 minutes earlier. The location of all the tangent points define a tangent point track that lies either to the north or south of the satellite track, with the 45/135 azimuth pair on one side and the 225/315 pair on the other.

This viewing geometry is illustrated in Figure 1, which shows the two tracks and the view directions for a set of positions along the tracks. The orientation of the tangent point tracks and view directions with respect to the latitude circles are fixed, but the section of the track that lies in daylight varies both seasonally and as the orbit precesses. The tangent point track used for observations is typically alternated from day to day in order to maximize latitude coverage. An example of the global coverage of HRDI measurements is shown in

Figure 3.

Because of the orbit precession, UARS performs a 180-deg. yaw maneuver every 36 days in order to keep the solar array pointed at the sun. The interval between the yaws defines periods of forward or backward flight as determined by the relative orientation of the x-axis and the UARS velocity vector. The 225/315 pair of azimuth angles lies on the same side of the satellite as the solar array, and is designated the warm side. Which of the two tangent point tracks is the warm side track thus changes after every yaw maneuver. Also, which of the two view directions in an azimuth pair is in the forward or backward direction changes after every yaw.

The HRDI mode of operation consists of a sequence of limb scans with the telescope alternately pointed in one of the two azimuth directions as described above. During a limb scan, the HRDI telescope zenith angle is varied in such a way that the line of sight tangent height covers a range from 10 to 40 km at 2.5-km intervals. The limb scans are performed in a sequence consisting of a pair of forward scans followed by a pair of backward scans. The first scan of each pair is made with the instrument tuned to observe a gamma band line in the O<sub>2</sub> spectrum, and the second with the instrument tuned to observe a B band line. A pair of different lines is chosen in order to maximize the information content as a function of altitude. The B band line is a strong line that provides information at high altitude, but saturates at low altitudes, while the gamma band line provides the best information at low altitudes.

The HRDI interferometer must be tuned in such a way that a given spectral line will appear on the detector. The tuning is changed when alternating between the B and gamma band line measurements, and is also changed between forward and backward look directions because of the large Doppler shift that results from the satellite motion. Each of these four different tunings has an associated unknown reference position as described above.

### 3.4 Sources of systematic error

The LOS velocity will contain systematic errors that arise from inaccurate knowledge of the model parameter inputs into the forward model calculation of the reference line shape  $C'_0$ . The LOS velocity error is with respect to the true LOS velocity that would be obtained if all the model parameters used in the forward model were correct, and there was no mea-

surement noise. Some of the model parameter estimates have a random error component, especially those that pertain to the atmospheric state, and will not contribute significantly to a systematic error when averages over a large set of LOS velocities is taken.

The main source of systematic error in the LOS velocities will arise from inaccurate knowledge of the reference positions, which are a function of the four different instrument tunings. In the calculations of the HRDI LOS velocities discussed in the next section, a fixed estimate of the reference positions that is correct to within 100 m/sec was used in the forward model. Since a wind velocity of 380 m/sec will shift the line center by the distance that separates adjacent channels on the detector, these estimates are correct to within a quarter of the channel separation.

Another potential source of systematic LOS velocity error arises from the pressure shift. The pressure shift increases with pressure, so those measurements whose signal has a significant contribution from the lower part of the atmosphere are most affected by it. The pressure shift therefore affects measurements taken with lines of sight with tangent heights below 20 km, and taken over regions with large surface or cloud top albedo. The pressure shift can also lead to LOS velocity error if the aerosol properties are incorrectly specified in the forward model. Some of these errors will vary randomly over a large set of LOS velocity samples. As will be shown below, there does appear to be a systematic bias between HRDI and GEOS LOS velocities that has an altitude dependence, and the source of this bias is possibly due to pressure shift effects. However, the bias between HRDI and GEOS could also be the result of a bias between the GEOS and true winds that depends on altitude.

A third source of LOS velocity error can arise from an incorrect characterization of the HRDI instrument in the forward model, particularly the sensitivity specification for each channel. These sensitivities can vary with the telescope azimuth because the optical system that transmits light from the HRDI telescope to the detector passes through the telescope axis. Inhomogeneities in the image that falls on the detector will be twisted as the telescope turns, and there is no way to incorporate this effect into the forward model. Once again, it will be shown below that there is a systematic bias between HRDI and GEOS LOS velocities that depends on the telescope azimuth and that may arise from inaccuracies in the HRDI forward model. The HRDI viewing geometry also depends on the telescope azimuth in a systematic way, as shown in Fig. 1, so it is also possible that the bias between HRDI and

GEOS is the result of a bias between GEOS and the true winds.

As a result of the dependence of HRDI/GEOS LOS velocity bias on azimuth, together with the dependence on tuning but neglecting the dependence on altitude, these biases therefore depend on 16 different configurations of the HRDI instrument. The characterization of the instrument configuration may be made in a variety of ways, as is made clear in Table 1. The line of sight of a measurement may occur on the warm or cold side of the satellite, and may be occur with the satellite flying forward or backward. The HRDI data used in the next section covers all of September 1994, and UARS underwent a yaw maneuver on September 12. Before the yaw, UARS was flying forwards.

Azimuth	Look direction	Side	Yaw	Track
45	Forward	Cold	Before	North
135	Backward	Cold	Before	North
225	Backward	Warm	Before	South
315	Forward	Warm	Before	South
45	Backward	Cold	After	South
135	Forward	Cold	After	South
225	Forward	Warm	After	North
315	Backward	Warm	After	North

**Table 1.** LOS configurations as characterized by the telescope azimuth, the line of sight look direction relative to the spacecraft velocity, the cold/warm side designation, whether the configuration was in effect before or after the yaw on Sept. 12, 1994, and whether the given configuration corresponds to an observation taken on the the north/south tangent point track as illustrated in Figure 1.

## 4 Determining HRDI LOS velocity biases

The mean LOS observation error or LOS observation bias

$$b_{los}^o = \langle \epsilon_{los}^o \rangle \quad (3)$$

is defined relative to the true state, i.e. where the observation error  $\epsilon^o$  is given by

$$\begin{aligned} \epsilon_{los}^o &= V_{los}^o - V_{los}^t \\ &= V_{los}^o - h(\mathbf{V}^t). \end{aligned} \quad (4)$$

Here  $V_{los}^o$  is the observed line of sight velocity calculated from the Doppler shift,  $V_{los}^t$  is the true LOS velocity using the the true wind vector  $\mathbf{V}^t$  at atmospheric model grid points, and

$h(\cdot)$  is the *observation operator* that operates on the wind field defined in the model grid space to give the LOS wind velocities at the observation location.

The observation operator is linear and consist of three operations or operators; 1-  $H_I$  a bilinear interpolation of the wind field to a profile wind at the longitude and latitude of the observation, 2-  $H_P$  a projection operator of the horizontal wind to the line of sight,

$$H_P = -u\cos(\phi) - v\sin(\phi), \quad (5)$$

where  $\phi$  is the viewing angle measured clockwise due south, and 3-  $H_K$  a vertical averaging using the LOS velocity kernel or contribution functions, Equation (2). The contribution functions, derived using the single scattering model described in section 3.2. The scattering model has 60 altitude levels, starting at 0.5 km, 1.0 km apart. and there are 13 LOS level measurements Figure 4 shows a typical set of averaging kernels or contribution functions for a 13 level wind measurement.

Since the observation error is defined with respect to the unknown true atmospheric state, an additional source of information is needed for its determination. Using collocated and time-coincident radiosondes observations would results in too few coincidences, and data limited to below 35 km. Instead, we use meteorological analyses linearly interpolated in time to the time of the HRDI observation, and take the difference between the observed LOS velocity and the simulated LOS velocity obtained by applying the observation operator on the meteorological wind analyses. These differences are analogous to 'observed-minus-forecast' (O-F) residuals, frequently used in data assimilation, with the difference that a meteorological analysis is used instead of a short-term forecast. Still, we will adopt this terminology for our differences, as they will strictly apply when assimilation of HRDI LOS velocities will take place. Observed-minus-forecast residuals,

$$\begin{aligned} d_{los} &= V_{los}^o - V_{los}^f \\ &= (V_{los}^o - h(\mathbf{V}^t)) - (V_{los}^f - h(\mathbf{V}^t)) \\ &= \epsilon_{los}^o - \epsilon_{los}^f \end{aligned} \quad (6)$$

are a combination of observation and forecast errors. The mean O-F residual is then

$$\begin{aligned} \langle d_{los} \rangle &= \langle \epsilon_{los}^o \rangle - \langle \epsilon_{los}^f \rangle \\ &= b_{los}^o - b_{los}^f \end{aligned} \quad (7)$$

We define  $b_{los}^o$  and  $b_{los}^f$  as the observation and forecast biases respectively. If the forecast bias is small enough to be neglected, as we will argue, then

$$b_{los}^o \approx \langle d_{los} \rangle \quad (8)$$

While there is no guarantee that the forecast can be neglected, we will argue that the mean O-F is independent of the forecast. In fact, we will show in the following section, that O-F biases computed using GEOS-DAS analyses or ECMWF analyses are very similar.

First let us examine the correlation between  $d_{LOS}$  and the LOS velocities. In Figure 5, a scatter plot between  $d_{LOS}$  and  $V_{los}^f$  is depicted in panel (a), and a scatter between  $d_{LOS}$  and  $V_{los}^o$  is depicted in panel (b), both for a single day (01-09-94). The O-F residual is largely uncorrelated with the forecast velocity while it shows a strong correlation with the observation velocity. In general plots like these are by no means proof that the bias originates mainly in the observations. It is entirely possible that the forecast greatly underestimates the magnitude of the wind, creating the large bias which appears to correlate with the observations. However, since the measurements are made in a number of different directions, it seems very unlikely that the forecast wind component in the LOS direction is always substantially smaller than the observed velocity. We are left with determining what part of this bias is the result of systematic forecast error. We investigate this by finding all of the significant measurement and retrieval parameters and plotting the errors against them.

If we plot this same set of O-F's vs the observation altitudes (Figure 6), we see that the variance increases substantially with altitude, but overall may be reduced if the bias is determined as a function of measurement parameters. Figure 7 shows O-F's for the same day in the B band (cold side, backward tuning) (a) and the gamma band (warm side, forward tuning) (b). The error variance for each band is qualitatively seen to be smaller than the whole data set, and only the gamma band suffers from a significant increase in variance with altitude. By separating out the observations by measurement parameters we can remove the bias as well as reduce the error variance.

In order to determine which parameters have the potential to significantly effect measurement and retrieval errors, we examine the derivation of the line-of-sight winds from HRDI measurements. Grassl *et. al.* (1995) derived the LOS wind velocity from the measurement of the centroid of an absorption line on the HRDI detector:

$$V_{los} = V - V_o(\nu, \phi) - \alpha(T - T_o) - f(t) - V_s \cos(\xi) \cos(\beta) - \frac{2\pi R_e}{T_e} \sin(\psi) \cos(\phi) \quad (9)$$

Here  $V_{los}$  is the retrieved line-of-sight wind component and  $V$  is the measured LOS wind. The rest of the terms are corrections in the wind for the zero wind reference  $V_o(\nu, \phi)$ , zero position adjustment for change in instrument temperature  $\alpha(T - T_o)$ , instrument drift due to changes in the space environment  $f(t)$ , the component of the spacecraft velocity in the LOS direction  $V_s \cos(\xi) \cos(\beta)$ , and the component of the Earth's rotation in the LOS direction  $\frac{2\pi R_E}{T_E} \sin(\psi) \cos(\phi)$ . Difficulty in estimating the zero wind reference may contribute significantly to the observation bias. The HRDI retrievals used global geophysical constraints, including, for example, the requirement that global winds be constant over short periods of time. That the biases remain so large indicates that the zero wind reference has not been successfully determined.

We expect that the rest of correction terms to be smaller, but not necessarily insignificant. The spacecraft velocity  $V_s$  is known to within  $1 \text{ ms}^{-1}$ , but errors in the elevation ( $\xi$ ) and azimuth ( $\beta$ ) angles make  $V_s \cos(\xi) \cos(\beta)$  relatively important. We expect there to be differences in bias between forward and backward scans. The HRDI alternates scans between the warm and cold sides of the spacecraft on alternate days. This means that the temperature correction term  $\alpha(T - T_o)$  should vary daily, and that any inaccuracies in the correction will cause a difference in bias between hot and cold side scans. There could also be a transient period at the start of each orbit when the instrument temperature is warming up that will effect this component of the correction. Inaccuracies in the long term drift term  $f(t)$  will appear as a slow rate of change of bias over time, and would need to be separated out from seasonal effects on bias. The contribution from the Earth rotation term is considered relatively small, but if significant it would appear as an east/west dependence in the bias.

Several other potential bias parameters do not appear explicitly in the correction equation. The altitude of the scan has a large impact on the measurement error. Lower altitude measurements involve contributions over a bigger range of altitudes, and tend to get a greater impact from cloud and surface reflection. These all make modeling of the zero wind reference more difficult and we therefore expect to get a larger variation in biases at lower altitudes.

At the very highest altitudes there is very little absorption/scattering and the accuracy of the measurements is again likely to be poor. The B and  $\gamma$  absorption bands also result in different errors, both random and systematic. The UARS satellite is turned around by a yaw maneuver about once a month in order to keep the solar panel pointed at the sun. As a result, the HRDI instrument must be rotated by  $180^\circ$  as well, and the azimuth angles relating to the forward/backward scans are reversed. This can also effect the zero wind reference correction term and the physical rotation of the instruments may alter the resulting measurement.

We have found a number of other parameters to have no significant effect on biases. These include latitude, longitude, solar zenith angle, scattering angle and view direction (relative to the earth).

We next consider the biases for the entire month of September 1994, separated into the 8 parameter permutations of forward/backward scans, and hot/cold side scans. In order to determine whether the bias is relatively constant over this short time interval we calculate a daily bias for each set of parameter values, shown in Figure 8. There is a substantial jump in the biases between Sept 11<sup>th</sup> and 13<sup>th</sup>, indicating that on these days at least, we have missed a significant parameter, while during the rest of the month the biases are relatively constant. As it happens, the UARS satellite underwent a yaw maneuver on September 12<sup>th</sup>, so that both hot/cold and backward/forward scans are reversed. Because the retrieval model must account for the motion of the satellite, there is a component of the bias introduced by this part of the model. When the orientation of the satellite is reversed, the backward/forward biases should also be reversed. This can be seen in varying degrees in the B and Gamma bands.

We therefore include a fourth parameter *before/after yaw*, which will ensure that the biases remain reasonably constant over a period of 10-15 days. In addition we include altitude as a fourth parameter, which is divided into 12 intervals.

The result is a set of 16 curves, each with 12 values, which show the bias dependence on these parameters. Figures 9,10 contain all of these curves, with the before/after yaw curves given on the same plots. The B band shows a very consistent relationship between the biases before and after the yaw maneuver, with respect to the forward/backward scans. On both the warm and cold sides the forward scan bias decreases ( $5\text{ms}^{-1}$ ) across the yaw.



while the backward scan bias increases ( $3 - 4 \text{ ms}^{-1}$ ). This strongly suggests that a bias of around  $5 \text{ ms}^{-1}$  can be attributed to the tuning

The bias correction scheme consists of subtracting off the appropriate bias for each set of parameters and altitude range. Once the bias is subtracted from the observations, the relative invariance of the biases seen in Figure 8 results in daily biases that remain well under  $1 \text{ m/s}$ . We find this for September 94 (when the bias was determined) and for the following month, which shows that any seasonal variations in the bias are not significant over a two month period. Since the spacecraft undergoes a yaw about once every six weeks, we simply need to recalculate the bias after each yaw maneuver occurs. Finally, replotting the O-F's for the bias corrected observations (Figure 11) shows that the random component of the error is substantially reduced. We will examine this component of the errors in detail in section 5.

## 5 Comparison of Bias Estimates Using GEOS-DAS ECMWF Analyses

The question arises as to what part of these biases originate in the analyses. The fact that the biases presented in the previous section are such strong functions of the observation parameters is an indication that a substantial part of the bias originates in either the measurement or retrieval. However, if the forecast component of the bias is overlooked, one risks the possibility that this bias will be incorporated into the assimilation process (Dee, 1998). In the absence of known zero bias observations for winds in the stratosphere, we use forecasts from other numerical weather prediction systems to estimate the size of the forecast bias.

Figure 12(a) shows the difference in *LOS* that is obtained using ECMWF and GEOS forecasts as a function of altitude for September 1, 1994, which is equivalent to the differences in *LOS* biases. For most of the altitudes, the difference in *LOS* bias is small ( $< 2 \text{ ms}^{-1}$ ). Therefore, for vertically averaged *LOS* winds, there is no substantial bias *between* ECMWF and GEOS forecasts. However, if we simply plot the difference between ECMWF and GEOS *u*-winds on the same day, averaged over the entire globe (Figure 12(b)), we see that the difference between the two forecasts is more substantial than the line-of-sight winds imply. The cause of this discrepancy comes from the nature of the line-of-sight observations themselves.

The u-wind bias between ECMWF and GEOS implies that the GEOS meridional wind is lower than the ECMWF wind by as much as  $12\text{ms}^{-1}$ . This difference does not show up in the line-of-sight bias calculation because the LOS winds measurements alternate between 4 directions, 90 degrees apart. When these are averaged over a large number of observations, roughly equally divided between the four directions, any systematic difference between winds in a fixed direction (u for example), will be averaged out. The reason that this kind of averaging does not remove the observational bias is that systematic measurement and retrieval errors are by definition, always in the line-of-sight direction. The implications here are extremely important for the assimilation of line-of-sight wind observations. When view directions alternate between directions that are 90 and/or 180 degrees apart forecast biases, which tend to be primarily meridional, are averaged out.

There may be some concern that since the actual bias correction scheme used here separates out warm/cold and forward/backward observations, these subsets may not completely average out forecast error. In order to check this, calculations of the bias difference between GEOS and ECMWF forecasts for each set of parameter values were carried out. In each case, the difference was never more than about  $1\text{m/s}$  confirming the absence of forecast bias in the observation bias corrections. There is therefore a clear advantage to carrying out assimilation on LOS winds rather than first carrying the retrieval to state variables (UV). If a bias correction scheme is carried out that considers all the important observational biases, an assimilation can be undertaken with the assumption that no forecast bias has been introduced.

## 6 Random Error Characteristics

The O-F plots in Figures 6,7 suggest a very large observation error variance, also depicted as the  $\Delta$  curve in Figure 13. This apparently large error variance is due to the fact that we have not properly removed error biases as a function of appropriate measurement parameters. If the biases are calculated for each of the parameter combinations before calculating the error variances, we get much smaller standard deviations. Figure 13 also shows standard deviation as a function of altitude for Gamma band, warm side, backward scan ( $\times$ ) and B band, warm side, backward scan (o) to be about half that of the entire data set. The existence of so many

measurement parameters most likely has increased the error variance of the measurements, but it also allows us to reduce that error by determining the relationship between the errors and the parameter space.

The observation and forecast error characteristics, as well as their correlation, if any, need to be specified for data assimilation. Generally because of lack of information, it is usual to assume that forecast and observation errors are uncorrelated, and that the primary observation measurements, which in this context would be the  $\gamma$  and B channel, would also be uncorrelated. In this section, however, we will actually establish if there is such correlations, and estimate the error variance of  $\gamma$  band observations, of the B band observations, and of the forecast (or background). This is made by using the method of maximum likelihood to estimate the correlation and variance values using O-F residuals, and due to the fact that we have nearly coincident  $\gamma$  and B band observations.

The  $\gamma$  band O-F residual,  $d^\gamma$ , and the B band O-F residual,  $d^B$ , are both a combination of forecast error,  $\epsilon^f$ , and their respective band measurement errors,  $\epsilon^\gamma$  and  $\epsilon^B$ , that is

$$\begin{aligned} d^B &= \epsilon^B + \epsilon^f \\ d^\gamma &= \epsilon^\gamma + \epsilon^f. \end{aligned} \quad (10)$$

For each azimuth angle, there are  $\gamma$  and B band observations that are made during the upward and downward scans (Or is it the reverse !!!!). These observations turn out to be never farther apart than 200 km (verify this!!!!), and thus are nearly coincident, so that we assume that the forecast error statistics is nearly the same. Collecting the  $\gamma$  band and B band observations at the same altitude into one vector, the O-F (or innovation) vector,

$$\mathbf{b} = [b^B, b^\gamma]^T \quad (11)$$

should have the following covariance matrix,

$$\mathbf{M} = \begin{bmatrix} A & C \\ C & B \end{bmatrix}, \quad (12)$$

where

$$\begin{aligned} A &= \langle b^B b^B \rangle = \sigma_f^2 + \sigma_B^2 + \sigma_f \sigma_B \rho_{fB} \\ B &= \langle b^\gamma b^\gamma \rangle = \sigma_f^2 + \sigma_\gamma^2 + \sigma_f \sigma_\gamma \rho_{f\gamma} \\ C &= \langle b^B b^\gamma \rangle = \langle b^\gamma b^B \rangle = \sigma_f^2 + \sigma_f \sigma_B \rho_{fB} + \sigma_\gamma \sigma_B \rho_{\gamma B} + \sigma_f \sigma_\gamma \rho_{f\gamma}. \end{aligned} \quad (13)$$

We note that there is six unknown statistical parameters.  $\sigma_f$ ,  $\sigma_B$ ,  $\sigma_\gamma$ ,  $\rho_{fB}$ ,  $\rho_{f\gamma}$ , and  $\rho_{\gamma B}$  that we will estimate from O-F residuals. For this end we use the method of maximum likelihood

estimation. Let  $\alpha$  be the vector of unknown parameters, i.e.  $\alpha = (\sigma_f, \sigma_B, \sigma_\gamma, \rho_{fB}, \rho_{f\gamma}, \rho_{\gamma B})$ . Assuming that the O-F are Gaussian distributed according to the law of large numbers, and serially uncorrelated, the join probability density of O-F's spanned over time  $t = t_1$  to  $t = t_K$  is given by

$$p(\mathbf{d}_1, \mathbf{d}_2, \dots, \mathbf{d}_K | \alpha) = \prod_{k=1}^K p(\mathbf{d}_k | \alpha), \quad (14)$$

where

$$p(\mathbf{d}_k | \alpha) = \frac{1}{\sqrt{2\pi \det(\mathbf{M}_k)}} \exp \left\{ -\frac{1}{2} \mathbf{d}_k^T \mathbf{M}_k^{-1}(\alpha) \mathbf{d}_k \right\}. \quad (15)$$

The maximum likelihood method consist in finding the parameter values that maximize the probability density (see Dee, 1999 for further discussion and implementation). Equivalently, instead of maximizing the probability density, one can minimize the logarithm of the probability density, known as the *log-likelihood function*

$$\begin{aligned} L_K(\alpha) &= \frac{\sum_{k=1}^K p(k)}{2} \log(2\pi) + \frac{1}{2} \sum_{k=1}^K \log[\det(\mathbf{M}_k(\alpha))] \\ &+ \frac{1}{2} \sum_{k=1}^K \mathbf{d}_k^T \mathbf{M}_k^{-1}(\alpha) \mathbf{d}_k \\ &= Cte + \frac{1}{2} \sum_{k=1}^K \log(AB - C^2) \\ &+ \frac{1}{2} \sum_{k=1}^K \frac{1}{AB - C^2} [d_B B d_B + 2d_B C d_\gamma + d_\gamma A d_\gamma], \end{aligned} \quad (16)$$

where Cte is a constant. Using Powell's minimization algorithm (Press *et al.*, 1992) and O-F residuals at the altitude of 25 km, the values of the parameters at the minimum are  $\sigma_f = 0.08$ ,  $\sigma_B = 0.45$ ,  $\sigma_\gamma = 0.17$ . We note that the observation and forecast errors are uncorrelated, i.e.  $\rho_{fB} = 0.00$ ,  $\rho_{f\gamma} = 0.00$ , and that the channel errors are mutually uncorrelated, i.e.  $\rho_{\gamma B} = 0.00$ .

The value of  $L_K(\alpha)$  about the minimum in each direction of the parameter space are depicted in Figure 14. The curvature at the minimum is a function of the accuracy of the parameter estimate (Dee 1999). The panels on variance indicates that the estimates for the channel error standard deviations,  $\sigma_\gamma$ ,  $\sigma_B$  are more accurate than the estimate of forecast error standard deviation  $\sigma_f$ . Likewise, the error correlation estimate between the channels is more accurate than between the channels and the forecast.

Having established that there is no correlation between error channels and between each channel error and the forecast error yields a simple prescription to obtain the observation error variance of each channel and of the forecast error variance. We take the covariance between these two O-F residual sets,  $cov(d^B, d^\gamma)$ , giving

$$cov(d^B, d^\gamma) = cov(\epsilon^B + \epsilon^f, \epsilon^\gamma + \epsilon^f) + var(\epsilon^f) \quad (17)$$

Similarly, computing the variance of  $d^n$  and of  $d^\gamma$  gives

$$\langle (d^B)^2 \rangle = \langle (\epsilon^B)^2 \rangle + \langle (\epsilon^f)^2 \rangle \quad (18)$$

$$\langle (d^\gamma)^2 \rangle = \langle (\epsilon^\gamma)^2 \rangle + \langle (\epsilon^f)^2 \rangle \quad (19)$$

Figure 15 shows the square roots of  $cov(d^B, d^\gamma)$ ,  $\langle (d^B)^2 \rangle$  and  $\langle (d^\gamma)^2 \rangle$ .

Finally, we raise the question as to what the bias correction scheme can do towards reducing the random component of the observation error. In Figure 16 we plot the error standard deviation of the O-F for the first four days of September 1994, before and after the bias correction is applied to the observations. At most altitudes,  $\sigma$  is reduced by about half. This reduction is really the result of our increased knowledge of the source of the errors, and how they vary with the observation parameters. In the upper curve, we assume no knowledge of the observation parameters and calculate the random errors for the complete set (although the altitude is retained as a parameter). In the lower curve, we make use of information on how the observation is made (B and  $\gamma$  band, etc), subtracting out biases before the random component is calculated. In theory, the remaining random errors are due to the fact that we still don't (and really can't ever) know everything about the source of errors in the observations.

The random errors depend on the parameter values so that if we plot them individually, we see that some cases have significantly less error than the data set as a whole. In Figure 17 the O-F standard deviations are plotted for the  $\gamma$  and B bands respectively, separated out by warm/cold side and forward/backward scans. The smallest error shown here ( $\gamma$  band at 10 km) is now less than half of the minimum for the bias corrected complete data set. This is not really an improvement since we have simply separated out the errors for the various parameter values. At the same altitude, the B band errors are much higher. Our conclusion

from this analysis is two-fold: First, because the random component is strongly dependent on observation parameters, we believe we can make the statement that they primarily originate in the observations rather than the forecast. This result reinforces the argument that we made previously using Figure 15 and equation 17. Second, the observation errors are now more than a factor of 4 smaller than the initial standard deviation (un-corrected). For example, at 10 km,  $\sigma$  for the  $\gamma$  band is between 10 and 15 m/s compared to 40 m/s. The observations can be assimilated separately from the rest, with some confidence that they can have some significant impact on assimilated upper air winds.

## 7 Conclusions and Discussion

A detailed error analysis of HRDI LOS observations were carried out using GEOS-DAS winds. This analysis considered both the systematic and random components of the error, and showed that by dividing the observations by measurement parameters one can extract detailed information about error sources. This insures that the bias correction scheme treats these biases as systematic *relative to each parameter* so that these components are not treated as random errors. Since the truth is unknown, we can never know exactly how much of the bias originates with the forecast. However, calculation of biases in terms of LOS winds makes the bias determination much easier. It's hard to imagine that a model forecast could be consistantly biased in the LOS direction. Even if a model consistantly overestimates the *magnitude* of the winds, the LOS measurements look in many directions, effectively cancelling out any forecast bias. This is why we don't see any systematic LOS difference between ECMWF and GEOS winds, even though the globally averaged zonal winds show a systematic difference as much as 14 m/s. This is also the reason why we don't use the actual LOS viewing direction (relative to a fixed direction) as an observation parameter. Wind direction is a geophysical parameter rather than an observational parameter, and we don't expect that a measurement in the meridional direction should have a consistantly different error than one in the zonal direction. One or both of these models have a significant zonal bias that *must not* be removed from the HRDI observations. The forecast bias must be dealt with during the assimilation process using a technique like the one mentioned in the

introduction. When we combine Figure 5 with the above arguments, we are confident that the LOS biases that we have removed are entirely observational bias.

We have also developed a method for separating observation error variance from forecast variance when satellite measurements are made using two uncorrelated absorption bands. We exploit the fact that HRDI is alternating between two different  $O_2$  absorption bands that are uncorrelated. One can then successfully isolate the forecast error variance. This result has significant implications for other satellite measurements where multiple bands may be used to measure the same quantity (MLS water vapor measurements are one example). Not only does this allow one to precisely quantify the observational error variance, but new information on the forecast error variance may be gleaned from the observation.

## References

- Boorman, P., R. Swinbank and D. Ortland, Met Office Technical Report No. 332, 2000.
- Bowman, K.P., Large scale isentropic mixing properties in the Antarctic polar vortex from analyzed winds, *J. Geophys. Res.* 98 23013-23027, 1993.
- Chen, P., Isentropic cross-tropopause mass exchange in the extratropics, *J. Geophys. Res.* 100, 16661-16673, 1995.
- Chen, P., J.R. Holton, A. O. Neill, R. Swinbank, Isentropic mass exchange between the tropics and extratropics in the stratosphere, *J. Atmos. Sci.* 51, 3006-3018, 1994.
- Dee, D.P., and A.M. da Silva, Data assimilation in the presence of forecast bias, *Quart. J.R. Meteorol. Soc.*, 124, 269-295, 1998.
- Grassl, H.J., W.R. Skinner, P.B. Hays, M.D. Burrage, D.A. Ortland, A.R. Marshall and V.J. Abreu, Atmospheric wind measurements with the High-Resolution Doppler Imager, *Journal of Spacecraft and Rockets*, 32, 169-176, 1995.
- Hays, P.B. and W.J. Abreu, Absorption line profiles in a moving atmosphere: A single scattering linear perturbation theory, *Journal of Geophysical Research*, 94, 18351-18365, 1989.
- Hays, P.B., V.J. Abreu, M.E. Dobbs, D.A. Gell, H.J. Grassl and W.R. Skinner, The high-resolution Doppler imager on the Upper Atmosphere Research Satellite, *J. Geophys. Res.* 98, 10713-10723, 1993.
- Hoppe, U.-P. and D.C. Fritts, On the downward bias in vertical velocity measurements by VHF radars, *Geophys. Res. Lett.*, 22, 619-622, 1995.
- Menard, R., S.E. Cohn, L.P. Chang and P.M. Lyster, Assimilation of Stratospheric Chemical Tracer Observations Using a Kalman Filter, Part I: Formulation, *Mon. Wea. Rev.*, 128, 2654-2671, 2000.
- Menard, R. and L.P. Chang, Assimilation of Stratospheric Chemical Tracer Observations Using a Kalman Filter, Part II:  $\chi^2$  Validated Results and Analysis of Variance and Correlation Dynamics, *Mon. Wea. Rev.*, 128, 2672-2686, 2000.
- Morris, G.A., J.F. Gleason, J. Ziemke, M.R. Schoeberl, Trajectory mapping: A tool for validation of trace gas observations, *J. Geophys. Res.* 105, 17875- 17894, 2000.
- Nastrom, G.D. and T.E. VanZandt, Biases due to gravity waves in wind profiler measurements of winds, *Journal of Applied Meteorology*, 35, 243-257, 1996.
- Ortland, D.A., P.B. Hays, W.R. Skinner, M.D. Burrage, A.R. Marshall, and D.A. Gell, A sequential estimation technique for recovering atmospheric data from orbiting satellites. In *The Upper Mesosphere and Lower Thermosphere: A Review of Experiment and Theory* eds. Johnson R.M. and T.L. Killeen, AGU Geophysical Monograph Series, Volume 87, 356 pp.,



1995.

Ortland, D.A., W.R. Skinner and D.A. Gell, Measurements of Stratospheric Winds by the High Resolution Doppler Imager, *Journal of Geophysical Research*, 101, 10351, 1996.

Parrish, D., and J. Derber, The National Meteorological Center's spectral statistical interpolation analysis system. *Mon. Wea. Rev.*, 120, 1747-1763, 1992.

Pierrehumbert, R.T. and H. Yang, Global chaotic mixing on isentropic surfaces, *J. Atmos. Sci.* 50, 2462-2480, 1993.

Press, W.H., S.A. Teukolsky, W.T. Vetterling, B.P. Flannery, *Numerical Recipes in Fortran 77*, Cambridge University Press, New York, 933 pp, 1992.

Rind, D and A. Lacis, The Role of the Stratosphere in Climate Change, *Surveys in Geophysics*, 14, 133-165, 1993.

Rood, R.B., A. Douglass, C. Weaver, Tracer exchange between tropics and mid latitudes, *Geophys. Res. Lett.* 19, 805-808, 1992.

Seo, K.-H. and K.P. Bowman, Levy flights and anomalous diffusion in the stratosphere, *J. Geophys. Res.* 105, 12295-12302, 2000.

Skinner, W.R., P.B. Hays, H.J. Grassl, D.A. Gell, M.D. Burrage, A.R. Marshall, D.A. Ortland, The high-resolution Doppler imager on the Upper Atmosphere Research Satellite, in *Optical Spectroscopic Techniques and Instrumentation for Atmospheric and Space Research*, edited by Jinxue Wang and Paul Hays, Proc. SPIE 2266, 281-293, 1994.

Stajner, I., L.P. Riishojgaard and R.B. Rood, The GEOS Ozone Data Assimilation System: Specification of Error Statistics, *Q.J.R. Meteorol. Soc.*, Accepted, 2000.

Waugh, D.W., Seasonal variation of isentropic transport out of the tropical stratosphere, *J. Geophys. Res.* 101, 4007-4023, 1996.

Waugh, D.W. et al., Transport of material out of the stratospheric Arctic vortex by Rossby wave breaking, *J. Geophys. Res.* 99, 1071-1088, 1994.

## 8 Figure Legends

- Figure 1:** HRDI measurement locations and view directions.
- Figure 2:** Schematic of the HRDI measurement geometry.
- Figure 3:** Typical HRDI coverage for a single day (Northern Winter).
- Figure 4:** Typical Contribution Functions.
- Figure 5:** O-F Residual vs. Line of Sight Velocity from  
(a) GEOS-DAS Forecast (b) HRDI Observation.
- Figure 6:** Altitude vs. O-F, September 1, 1994.
- Figure 7:** Altitude vs. O-F, B band, backward tuning, cold side (a),  
 $\gamma$  band, forward tuning, warm side (b), September 1, 1994.
- Figure 8:** Mean O-F calculated daily for the month of  
September 1994. biases are separated in to 8 parameter combinations,  
forward/backward scans, warm/cold side scans, and B (a) and  $\gamma$  (b)  
bands.
- Figure 9:** September 1994 Biases for B band, before and after the  
September 12 yaw maneuver. Cold side, forward tuning (a)  
and cold side backward tuning (b) Warm side, forward tuning (c) and  
warm side backward tuning (d).
- Figure 10:** September 1994 Biases before and after the September 12 yaw  
maneuver for the gamma band. Cold side, forward tuning (a)  
and cold side backward tuning (b) Warm side, forward tuning (c) and  
warm side backward tuning (d).
- Figure 11:** O-F vs altitude for bias corrected LOS observations  
September 1 1994.
- Figure 12:** Difference in mean O-F using GEOS and ECMWF forecasts with  
Line-of-Sight (LOS) observations (a) and globally averaged difference  
between GEOS and ECMWF zonal winds (b).
- Figure 13:** Error standard deviations as a function of altitude for:  
complete data set ( $\Delta$ ). Gamma band, warm side, backward scan ( $\times$ ).

B band, warm side, forward scan (o), Sept. 1-4, 1994 (all before the yaw maneuver).

**Figure 14:** Loglikelihood near the minimum.

**Figure 15:** O-F residual covariance of B, $\gamma$  band O-F, and standard deviations for the individual absorption bands.

**Figure 16:** Standard deviation as a function of altitude for the O-F residual before and after carrying out the bias correction, Sept. 1-4, 1994.

**Figure 17:** O-F standard deviation as a function of altitude for the O-F residual for the  $\gamma$  (a) and B (b) bands. The errors are further separated by forward/backward scans and warm/cold side.

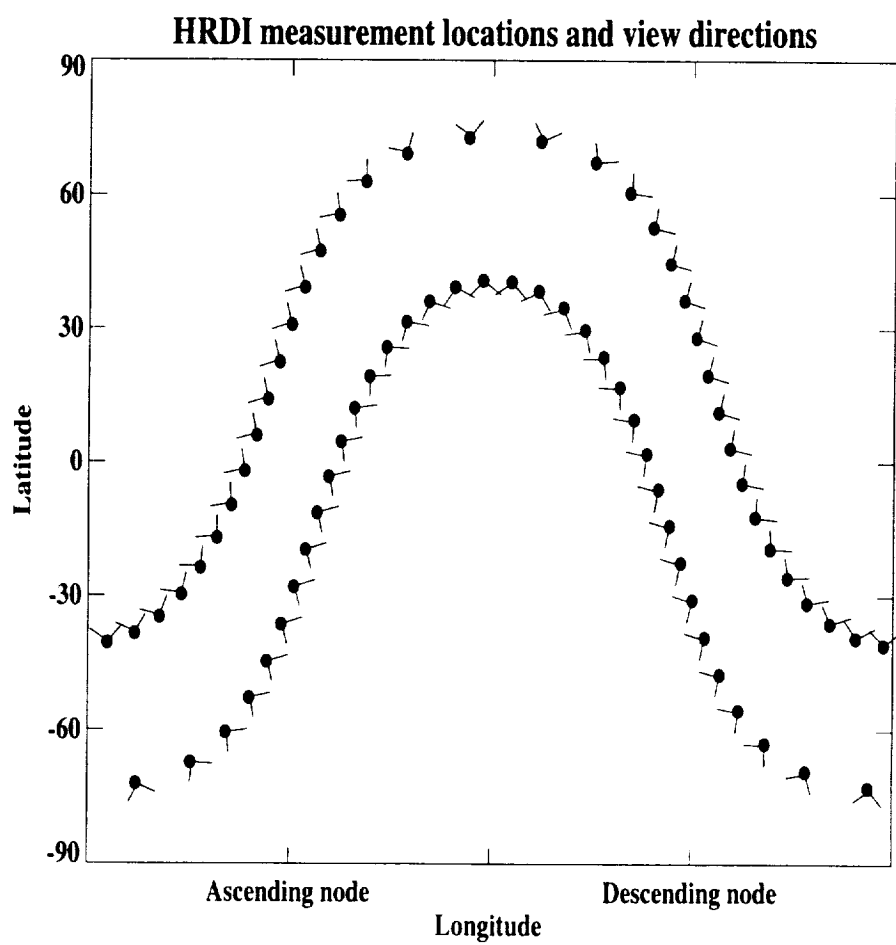


Figure 1:

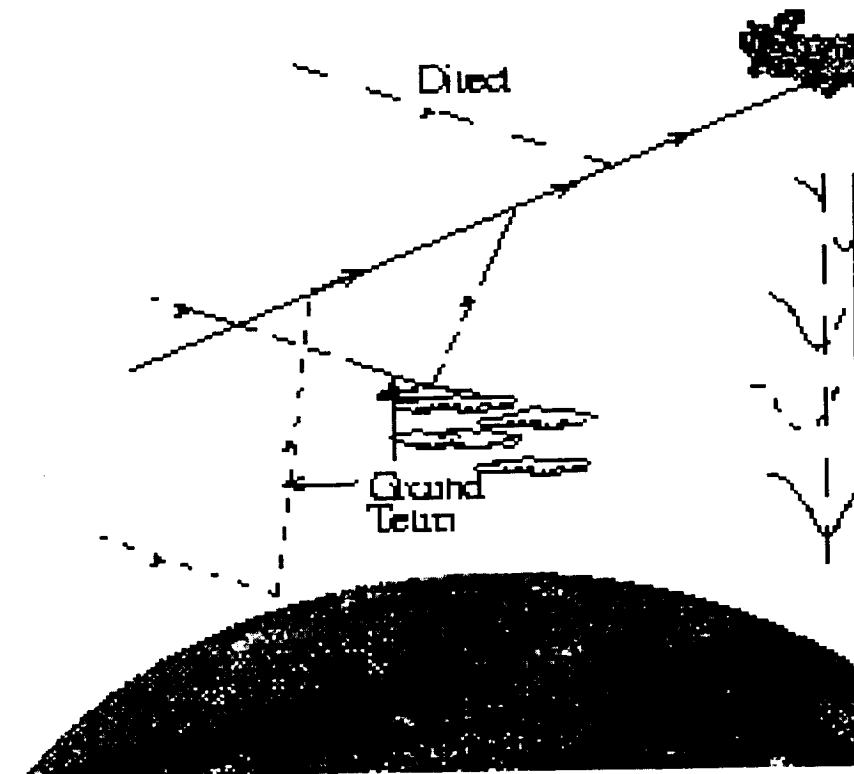


Figure 2: Schematic of the HRDI measurement technique.

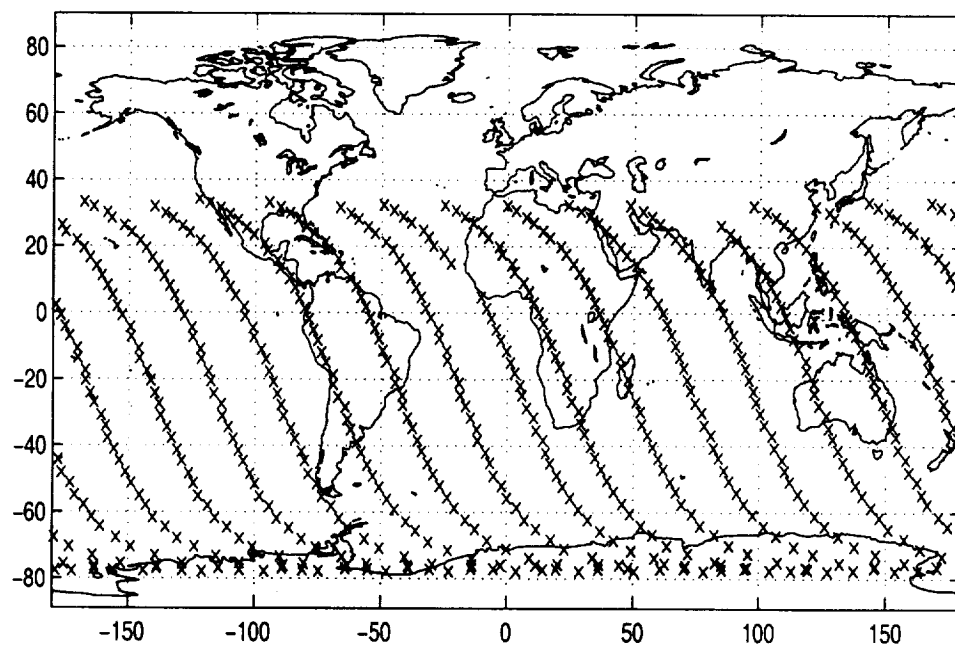


Figure 3: Typical HRDI coverage for a single day (Northern Winter)

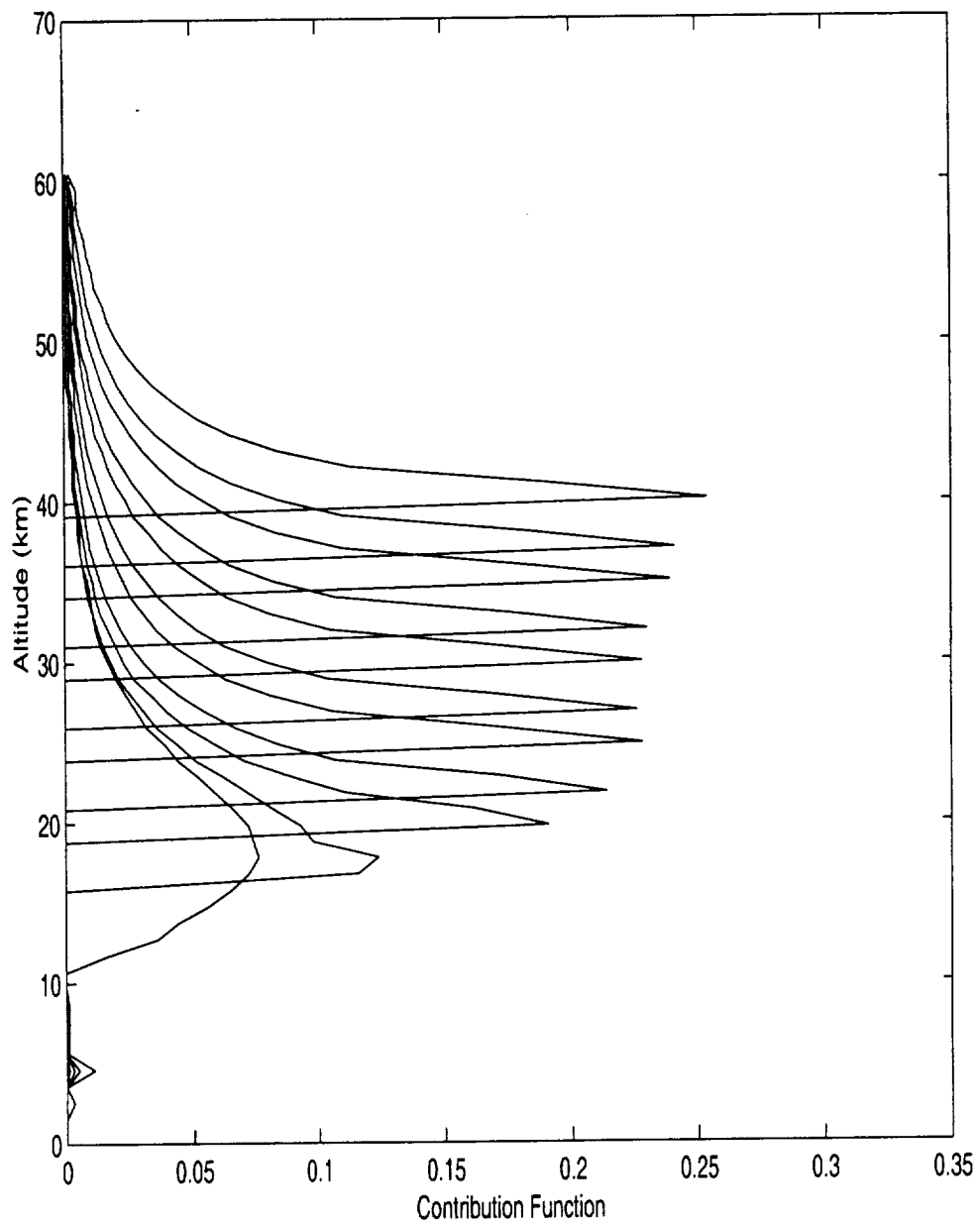


Figure 4: Typical Contribution Functions

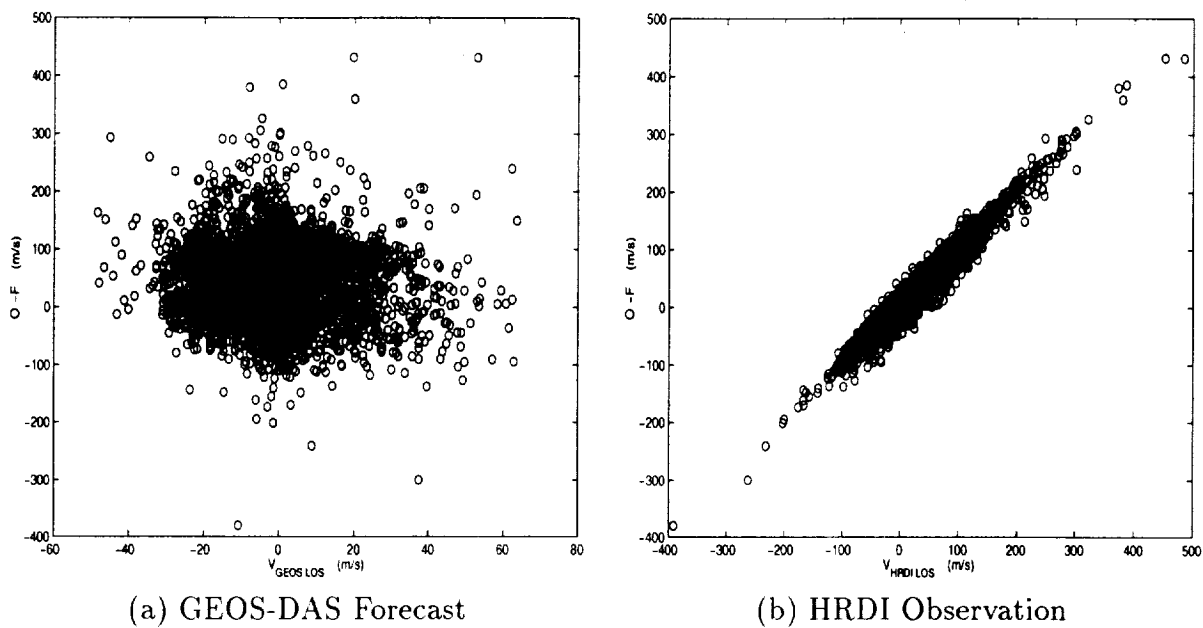


Figure 5: O-F Residual vs. Line of Sight Velocity

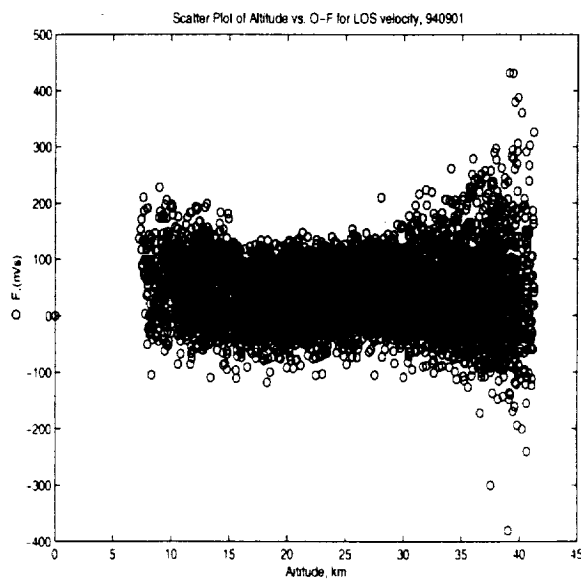


Figure 6: Altitude vs. O-F, September 1, 1994



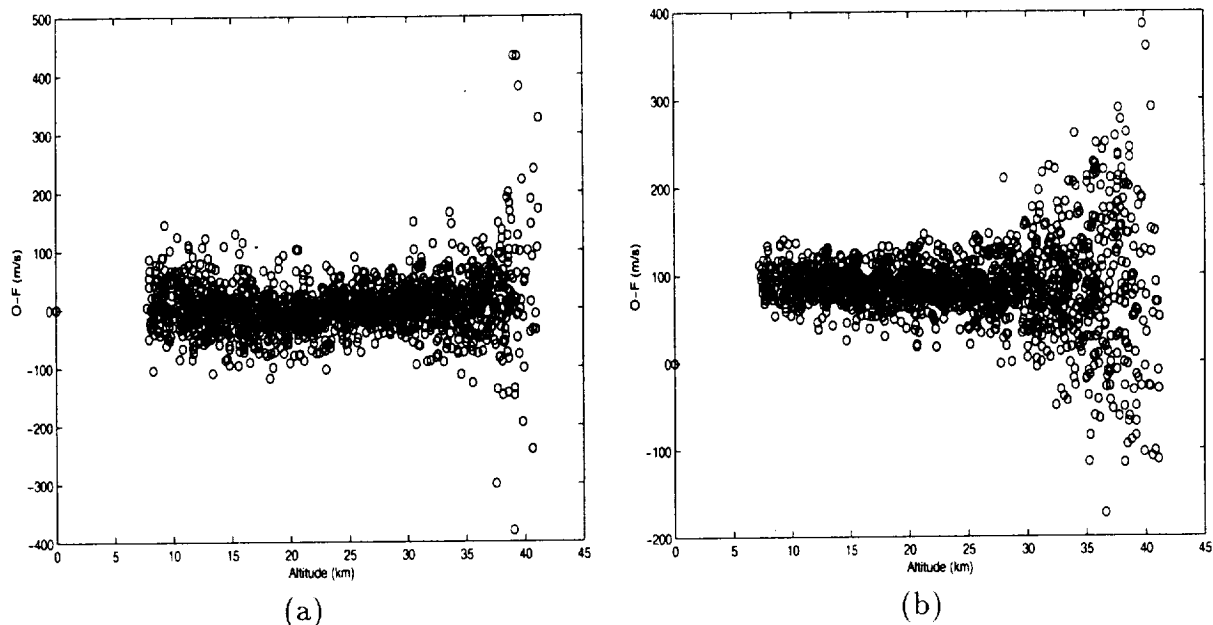


Figure 7: Altitude vs. O-F, B band, backward tuning, cold side (a),  $\gamma$  band, forward tuning, warm side (b), September 1, 1994

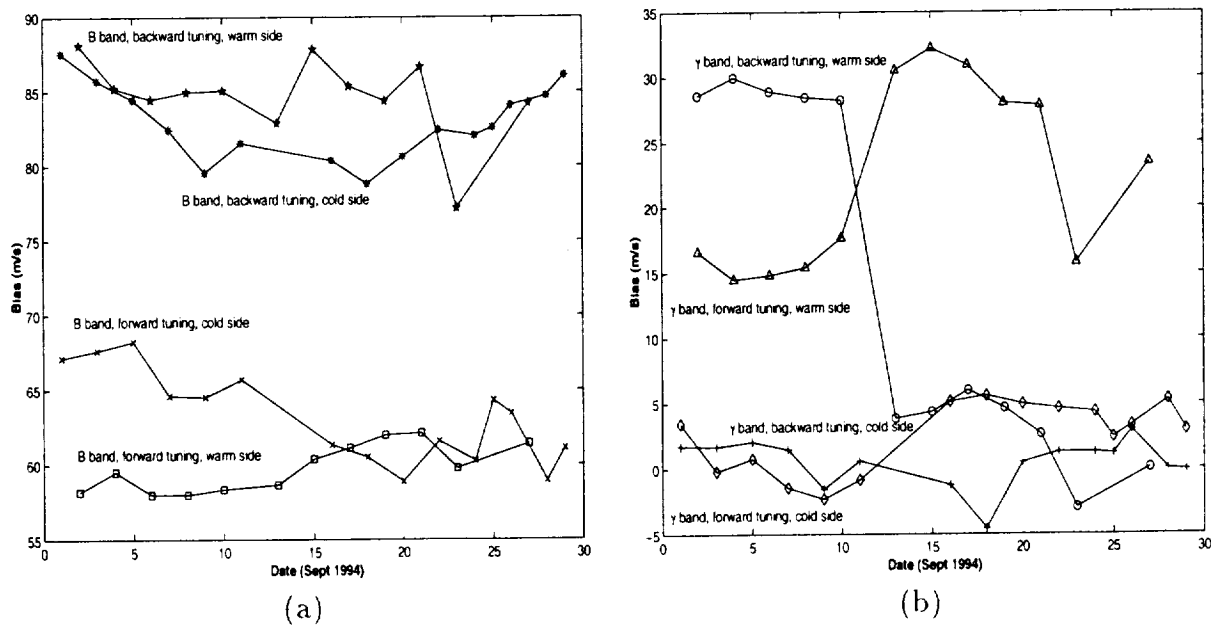


Figure 8: Mean O-F calculated daily (daily bias) for the month of September 1994. biases are separated in to 8 parameter combinations, forward/backward scans, warm/cold side scans, and B (a) and  $\gamma$  (b) bands.

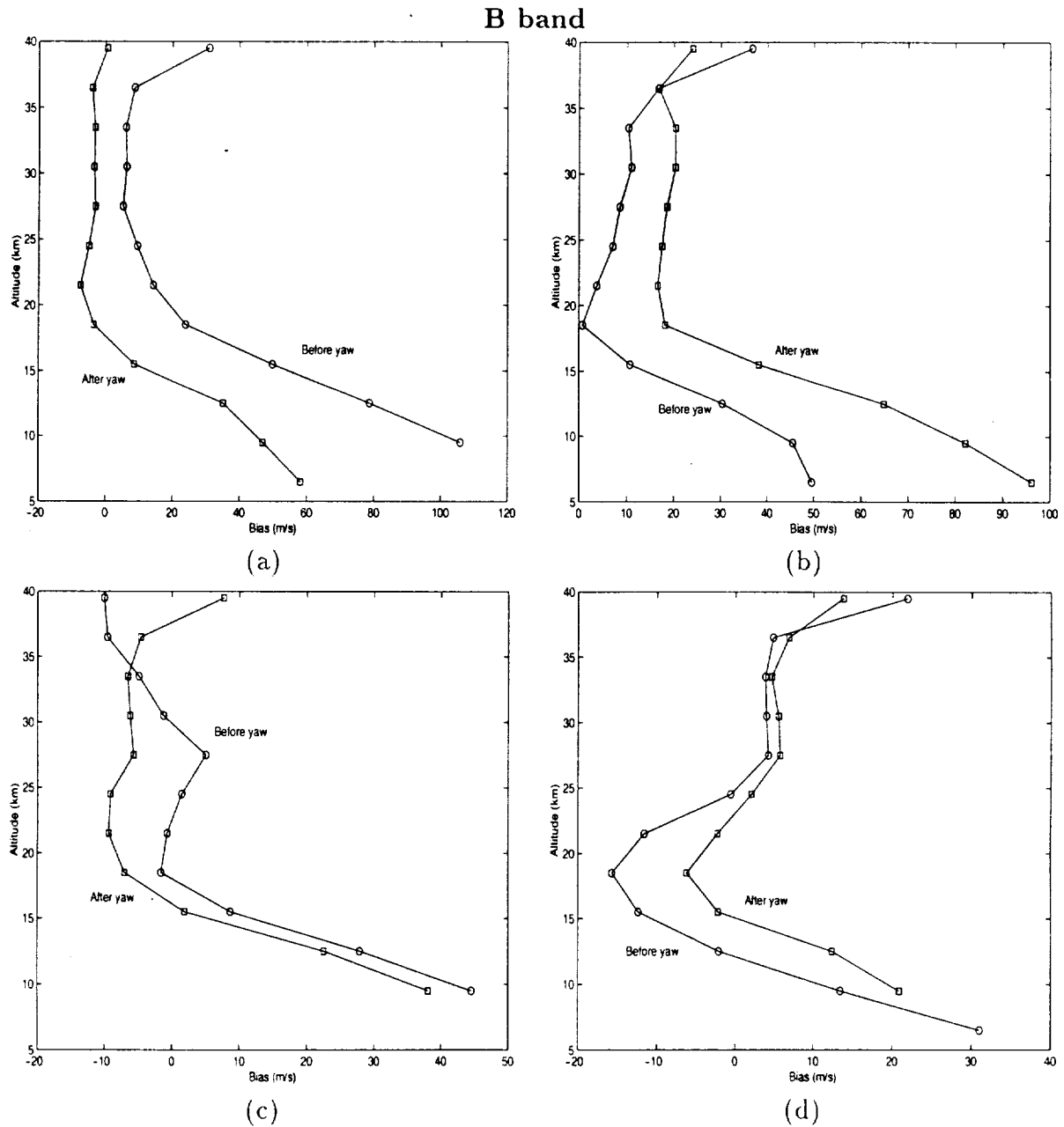


Figure 9: September 1994 Biases for B band, before and after the September 12 yaw maneuver. Cold side, forward tuning (a) and cold side backward tuning (b) Warm side, forward tuning (c) and warm side backward tuning (d).

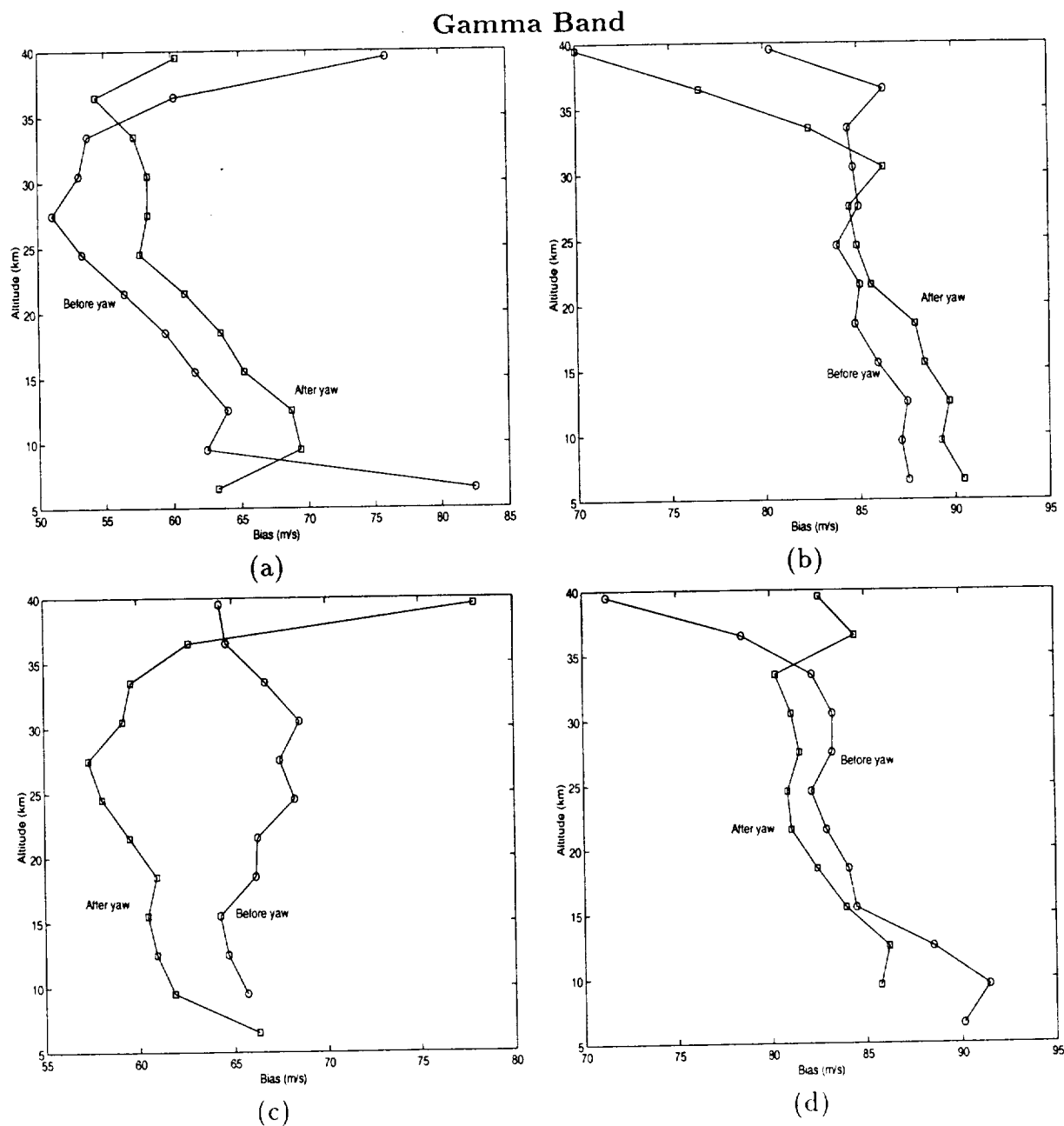


Figure 10: September 1994 Biases before and after the September 12 yaw maneuver for the gamma band. Cold side, forward tuning (a) and cold side backward tuning (b) Warm side, forward tuning (c) and warm side backward tuning (d).

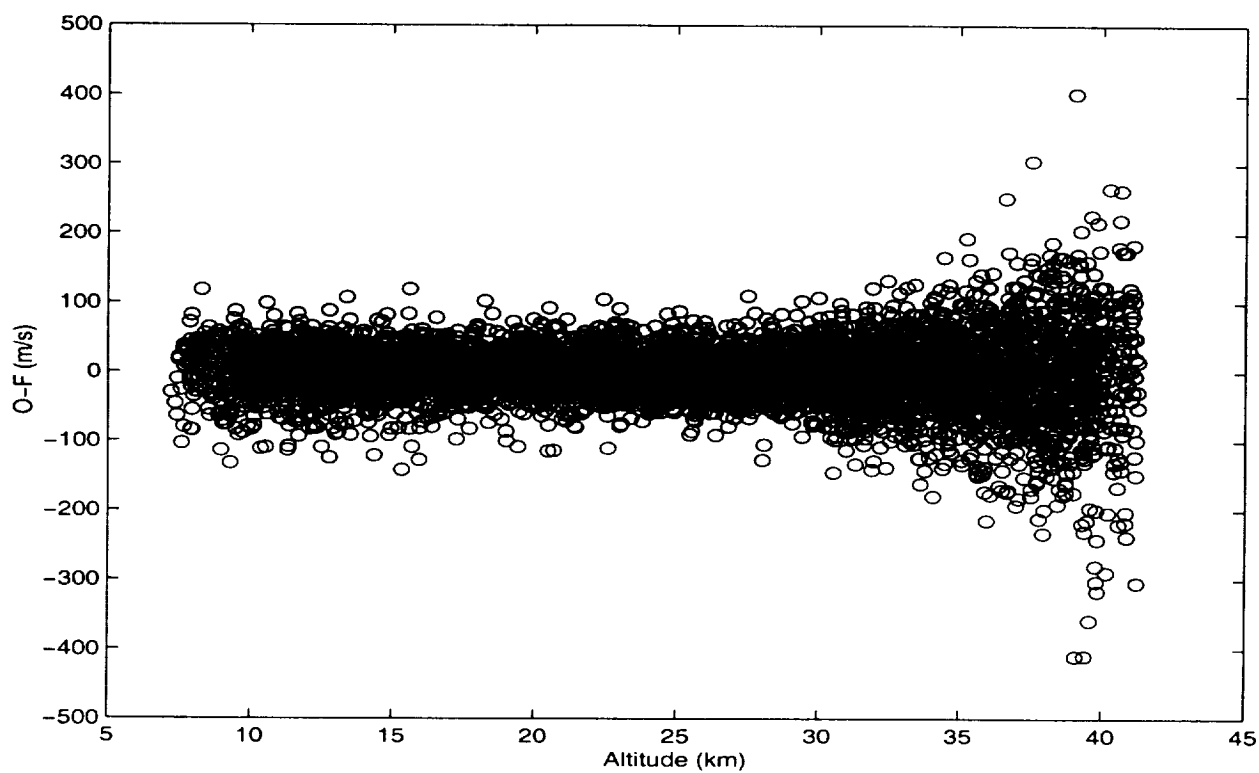


Figure 11: O-F vs altitude for bias corrected LOS observations September 1 1994.

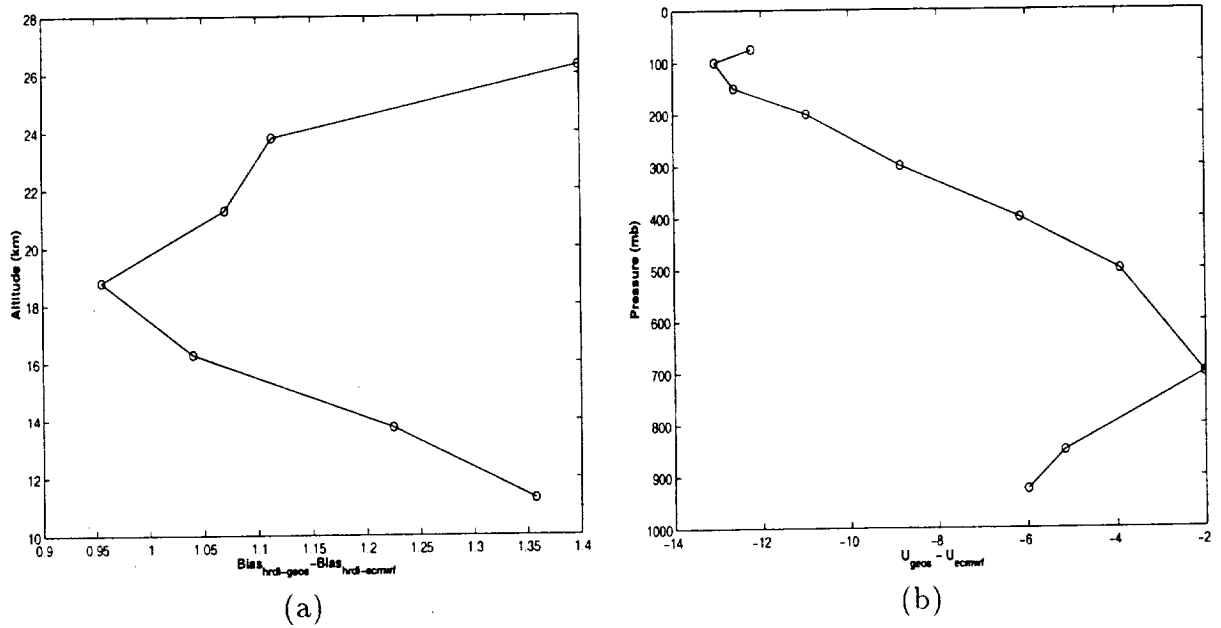


Figure 12: Difference in mean O-F using GEOS and ECMWF forecasts with Line-of-Sight (LOS) observations (a) and globally averaged difference between GEOS and ECMWF zonal winds (b).

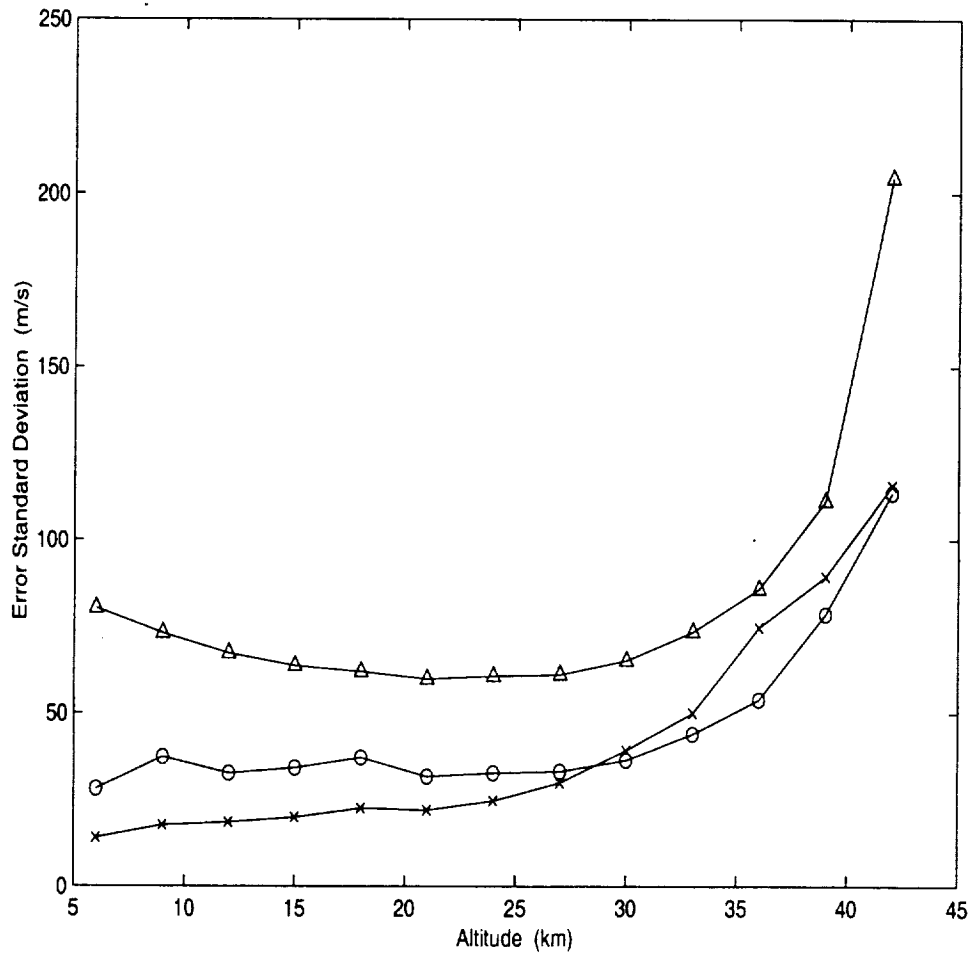


Figure 13: Error standard deviations as a function of altitude for: complete data set ( $\Delta$ ), Gamma band, warm side, backward scan ( $\times$ ), B band, warm side, forward scan ( $\circ$ ), Sept. 1-4, 1994 (all before the yaw maneuver)

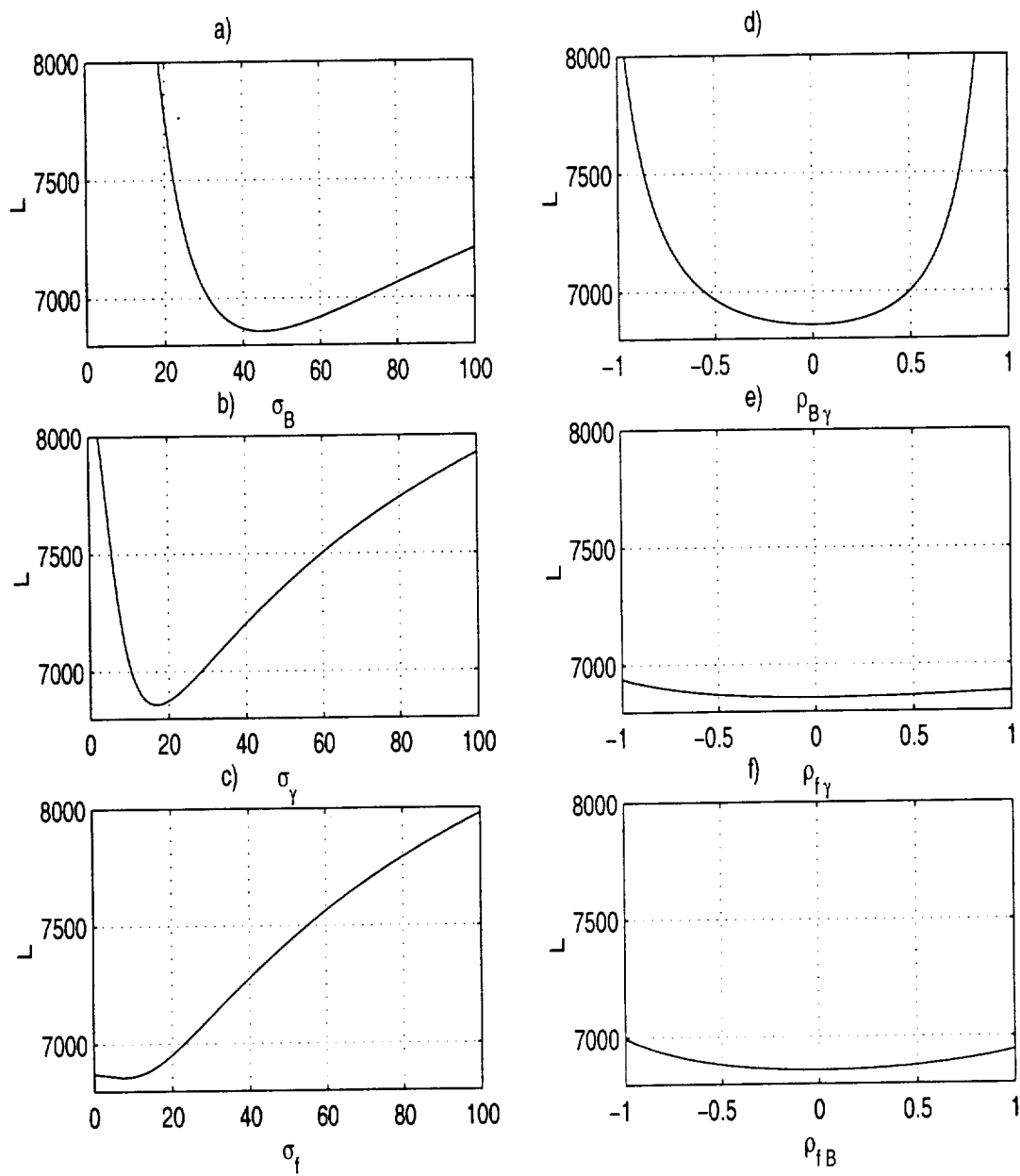


Figure 14: Loglikelihood near the minimum

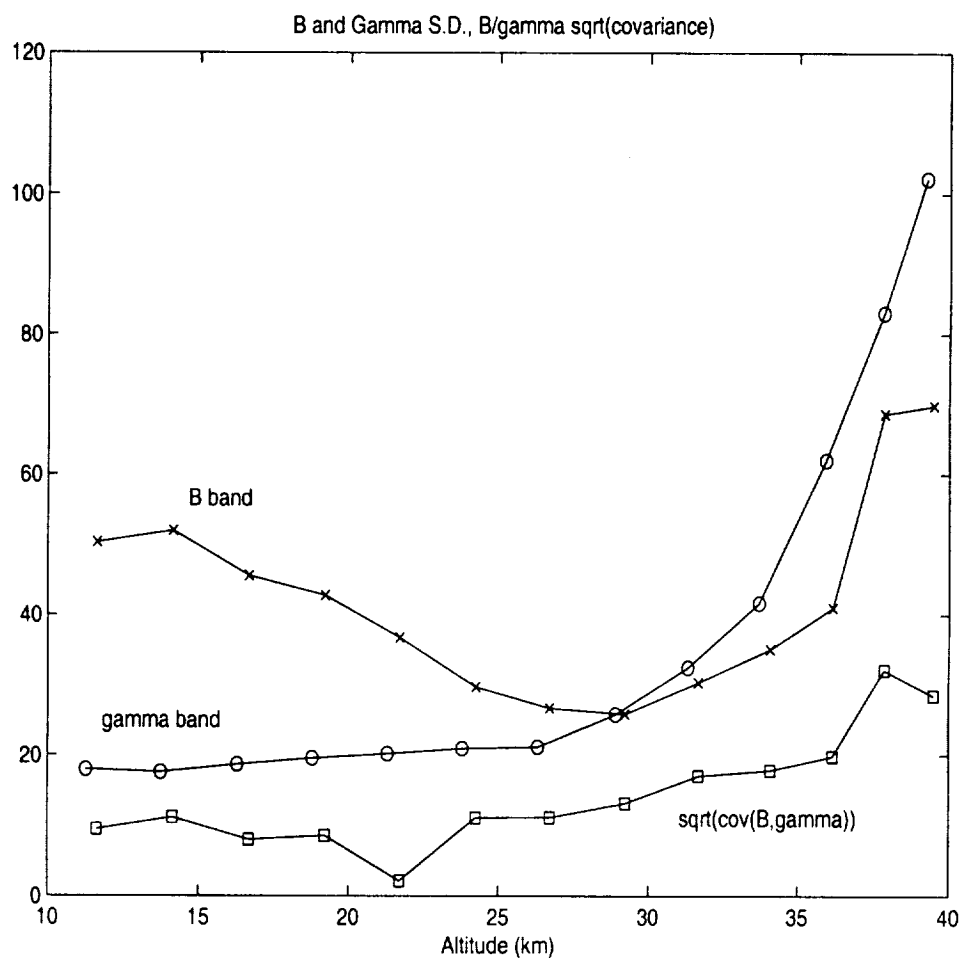


Figure 15: O-F residual covariance of B, $\gamma$  band O-F, and standard deviations for the individual absorption bands



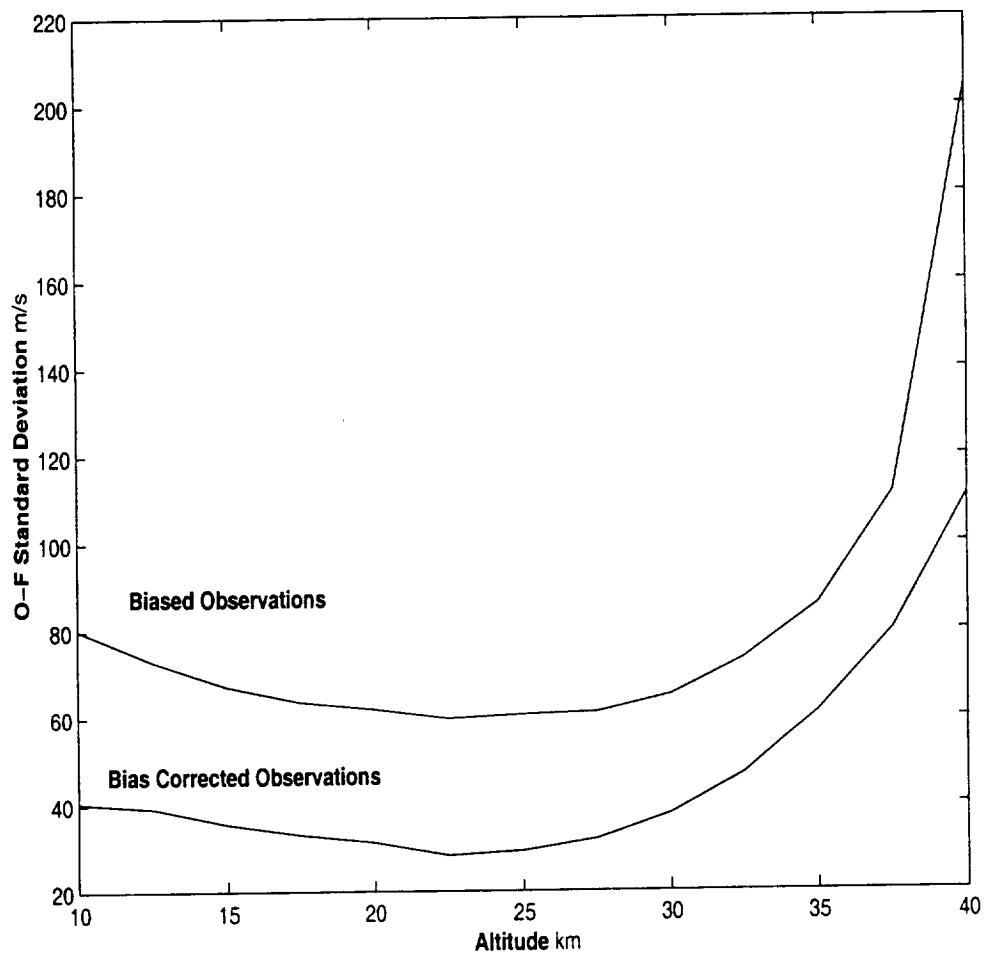


Figure 16: Standard deviation as a function of altitude for the O-F residual before and after carrying out the bias correction, Sept. 1-4, 1994

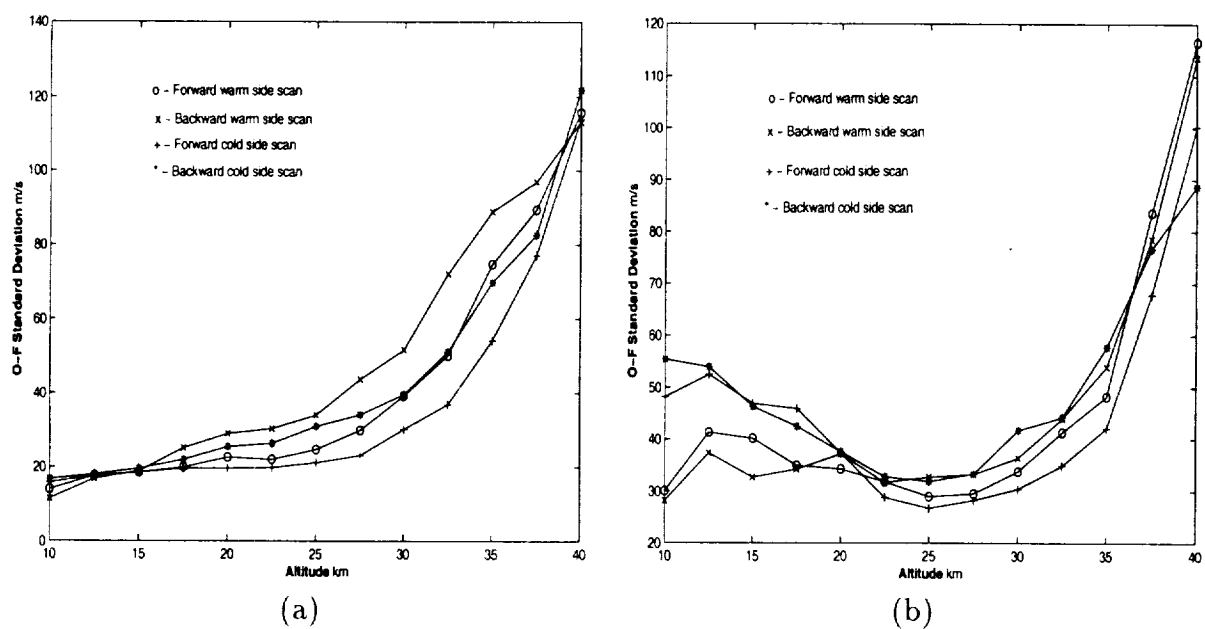


Figure 17: O-F standard deviation as a function of altitude for the O-F residual for the  $\gamma$  (a) and B (b) bands. The errors are further separated by forward/backward scans and warm/cold side